Int. J. Electrochem. Sci., 17 **(2022)** Article Number: 221042, doi: 10.20964/2022.10.42

International Journal of
ELECTROCHEMICAL
SCIENCE
www.electrochemsci.org

Short Communication

The effect of niobium doping on the corrosion resistance of stainless steel coatings

Zhongjie Wang, Junwen Zheng, Xin Zhang[*]

School of Materials Science and Engineering, Yancheng Institute of Technology, Yancheng, 224051, China
[*]E-mail: xinzhang@ycit.edu.cn

Received: 13 July 2022 / *Accepted:* 15 August 2022 / *Published:* 10 September 2022

The corrosion behavior of stainless steel wear-resistant coatings present a key challenge limiting the performance of their products and commercial viability. In this work, the influence of elemental niobium (Nb) on the microstructure and corrosion behavior of stainless steel coatings was surveyed via morphology characterization and electrochemical workstation. The corrosion resistance mechanisms were investigated through first-principle calculations. The experimental results show that the diffusion of elements during the melting pool reaction promotes the precipitation of carbides, and energy dispersive spectroscopy (EDS) line scans indicated pronounced Nb segregation near the grain boundaries. The corrosion resistance of stainless steel coatings was obviously improved by Nb doping, and a highest self-corrosion potential of -0.760 V and a relatively low corrosion current density of 3.481 $\mu A\cdot cm^{-2}$ was observed. Furthermore, first-principle calculations revealed that Nb segregation raised the activity of iron (Fe) surfaces and enhanced the adsorption of oxygen (O), thereby promoting the formation of oxide films. This work demonstrated a Nb doping to promote the formation of an oxide film on the surface of stainless steel coatings, thereby improving the corrosion behavior of high-Nb stainless steel coatings.

Keywords: Stainless steel wear-resistant coating, High-Nb, Corrosion resistance, First-principle calculations

1. INTRODUCTION

Stainless steel wear-resistant coatings have been widely applied as surface strengthening of iron (Fe)-based materials due to their outstanding characteristics, such as high strength, hardness as well as excellent thermal shock and wear resistance [1-3]. However, when corrosive media penetrated the coatings or small defects (scratches or impurities etc.) appeared on the coatings local corrosion occurred [4]. Stainless steel wear-resistant coatings fail quickly as a result [5]. Therefore, improving the corrosion resistance of stainless steel wear-resistant coatings is crucial when employing them for future applications.

To date, a number of methods have been proposed for improving the corrosion resistance of stainless steel wear-resistant coatings, including surface modification and elemental doping. In detail, Zhang investigated the AISI 420/VC metal matrix composites with different weight percentage (0 wt.% – 40 wt.%) of vanadium carbide (VC) fabricated on a mild steel A36 by a high power direct diode laser [6]. The results indicated that the erosion resistance of the cladded layer was improved after the introduction of VC. Wang obtained a golden, yellow-colored cerium conversion coating on a 304 stainless steel surface by immersing the steel in a solution containing cerium(III), potassium permanganate ($KMnO_4$) and sulfuric acid, and the experimental results indicated that the corrosion resistance for the conversion coated 304 SS in 3.5% sodium chloride (NaCl) solution increased markedly[7]. Typically, surface modification could be a potent strategy for improving the corrosion resistance performance of stainless steel. Nevertheless, film failure due to interfacial stress is a challenge that cannot be completely avoided. It is worth noting that trace alloying element doping can effectively reduce interfacial stress while improving corrosion resistance [8-10]. Among them, elemental niobium (Nb)-doped stainless steel has attracted much attention because of its excellent wear and corrosion resistance. However, the corrosion behavior and corrosion resistance mechanisms of elemental Nb doped stainless steel is still not completely clear. As the Nb content is very low, the conventional experimental solutions for the analysis of the effect of Nb on the corrosion resistance of stainless steel are considerably limited.

Fortunately, first-principle calculation technologies offer an unprecedented opportunity to address these questions. Han studied the effects of alloying elements in popular steels on the oxidation and dissolution corrosion of the surface of γ-Fe(III), the results showed that elemental Nb tended to migrate to the Fe(III) surface [11]. Bell showed that low oxidation state charged Nb ions (2^+ or 3^+) balance the build-up of positive space-charges in the oxide layer, increasing O vacancy and electron mobility, leading to near-parabolic corrosion kinetics and a reduced hydrogen pick-up [12]. Yuan showed that attractive/repulsive interactions were observed between O and alloy atoms with atomic numbers below/above Fe [13]. Based on these results, it can be expected that oxidation occurs mainly in the deviated regions of the low atomic number atoms on the Fe(100) surface. These studies explain, to some extent, the anti-corrosive effect of Nb, but they are still not satisfactory, especially the effect of Nb concentration on the anti-corrosion property.

In this work, the effect of Nb content on the corrosion resistance of the coating was investigated by generating an iron-based composite overlay layer on Cr5 steel plate using an overlay welding technique. The surface morphology of the coating was characterized using optical microscopy (OM) and scanning electron microscopy (SEM). The interfacial element changes were analyzed by the line scan of energy dispersive spectroscopy (EDS). The corrosion resistance of the coating with different concentrations of Nb were studied by an electrochemical workstation and immersion corrosion test. In addition, the first-principle calculations were used to study the adsorption between Nb-doped Fe surfaces and the O atom. The influence of Nb doping on the O adsorption was investigated by analyzing the adsorption energy, work function, charge density difference and Mulliken population analysis.

2. EXPERIMENTAL AND COMPUTATIONAL DETAILS

2.1 Coating Preparation

A Cr5 substrate (100 mm × 100 mm ×5 mm) was dried after rust removal by ultrasonic cleaning. The elemental composition of the substrate is reported in Table 1. Nb additive stainless steel coating was fabricated via transferred arc welding (PTA) technology [14]. The chemical composition of the coating is listed in Table 2, the powders were supplied by the Institute of New Materials, Guangdong Academy of Sciences. Before PTA coating, all the cladding powders were dried at a temperature of 120°C for 2 h. The PTA process was performed using a Eutronic Gap 2501 DC apparatus with a co-axial powder injection system. The PTA cladding was completed in multilayers on the Cr5 steel substrate and the optimized main processing parameters were as follows: weld current 140 A, weld speed 3 mm/s, shielding argon gas flow rate 20 L/min, and the distance between the torch and surface of the coating layer was 10 mm. Subsequently, different PTA Nb additive stainless steel cladding specimens with 0%, 3% and 5% Nb were labeled as 1#, 2# and 3#, respectively.

Table 1. Elemental content of Cr5 steel substrate

Elements	Cr	Mo	Si	Mn	Ni	P	S	Fe
Content (%)	5	0.5	0.12	0.42	0.20	≤0.03	≤0.03	balance

Table 2. Elemental content of Nb additive stainless steel coating (wt.%)

No.	Nb	Cr	Si	Mn	C	Ti	Fe
1#	0	7	1	1	1.25	0.3	balance
2#	3	7	1	1	1.25	0.3	balance
3#	5	7	1	1	1.25	0.3	balance

2.2 Materials characterization

A comprehensive microstructural evaluation of the three PTA specimens was analyzed by OM (Axio Imager.M2m, USA) and SEM (XL-30, Philips, Japan) equipped with an energy dispersive spectrometer (EDS).

The immersion corrosion in 3.5 wt% NaCl solution was conducted in accordance with the national standard GB10124–88. The area of corrosion zone was 10 × 10 mm^2, and the other parts were coated by phenolic resin. The test time was 30 h according to the pre–corrosion test, and the corrosion solution was changed every 10 h. The corrosion resistance of coatings was evaluated by the weight loss method, the weight loss ΔW before and after the corrosion test was measured using an electronic scale with the accuracy of 0.1 mg, and the corrosion rate was:

$$V = \frac{\Delta W}{A \times t \times \varphi} \qquad (1)$$

where A was the corrosion area; t was the corrosion time; and Φ was the coating density.

2.3 Electrochemical measurements

Electrochemical measurements were performed using a CH604E electrochemical workstation from Shanghai CH Instruments. The counter electrode, working electrode and reference electrode were Pt electrodes (99.99%), a specimen with a cross-sectional area of 8 mm × 8 mm, and a saturated glycerol electrode, respectively. The tests were performed in an open system at a temperature of 25°C ± 0.1°C, using a 3.5% NaCl solution as the electrolyte. The tests were recorded for potential curves from -1.0 V to 0.3 V (scan rate: 0.2 mV/s). The corrosion potential (E_{corr}) and corrosion current density (I_{corr}) were determined using the Tafel extrapolation method.

The electrochemical impedance spectra (EIS) were measured at the open circuit potential (OCP), a frequency ranging from 10 kHz to 10 mHz with a potential amplitude of 10 mV was used. The impedance data were analyzed using the ZView2 software [15].

2.4 First-principle calculation details

Based on density-functional theory, first-principle calculations were performed using the CASTEP code [16]. The ultrasoft pseudopotentials were used to study the ion-electron interactions[17] and the exchange correction energy was evaluated with the local density approximation (LDA) [18]. The cut-off energy of the plane-wave was 500 eV and a 7×7×1 k-points grid centered at the k-point was used following the Monkhorst-Pack method [19], the force convergence precision and energy were chosen as -0.01 eV/Å and 10^{-6} eV/cell, respectively. The Fe(100), Fe(110) and Fe(111) surface was modeled using a (2 × 2) five-layer slab supercell with the bottom two layers frozen. Each slab was separated by a vacuum of 15 Å to minimize the interactions between the images.

3. RESULTS AND DISCUSSION

3.1 Microstructure and surface morphology

The OM of different specimens is shown in Figure 1. It can be seen that all specimens have no obvious defects and cracks. With a further increase in Nb content to 3%, the amount of carbide precipitation gradually increases, and the grain boundary of the matrix organization gradually blurs and small grains appear, which is because the diffusion of elements in the melt pool reaction process promotes the precipitation of carbide. With the increase in Nb content, the quantity of precipitated carbide increases, and the grain boundary is a channel for rapid diffusion of atoms, so a large amount of carbide precipitation along the grain boundary makes the grain boundary gradually blurred and contributes to grain refinement.

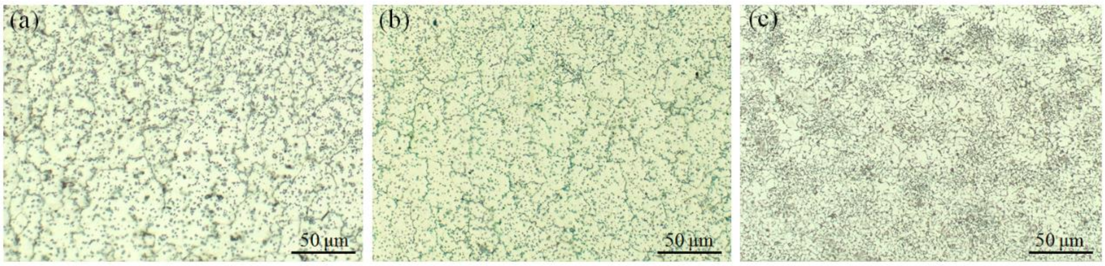

Figure 1. OM of different specimens (a) 1#; (b) 2#; (c) 3#.

Figure 2 shows the microstructure of the overlay specimens with different Nb content. From Figure 2, it can be found that the number of carbides precipitated in the overlay layer increases gradually with the increase in the Nb content. This is mainly because the alloying elements in the wire are dissolved in the molten pool, and the fluidity of the molten pool drives the redistribution of the elements in the molten pool [20]. The higher the Nb content, the wider the distribution in the molten pool and the more contact with the C atoms, and the wire composition provides a sufficient amount of C to react with Nb, so as the Nb content increases, the number of NbC increases and precipitates with the cooling of the molten pool. Subsequently, titanium carbide (TiC) is used as the nucleation center, and it continuously aggregates around the TiC to finally generate (Nb, Ti)C composite carbide [21].

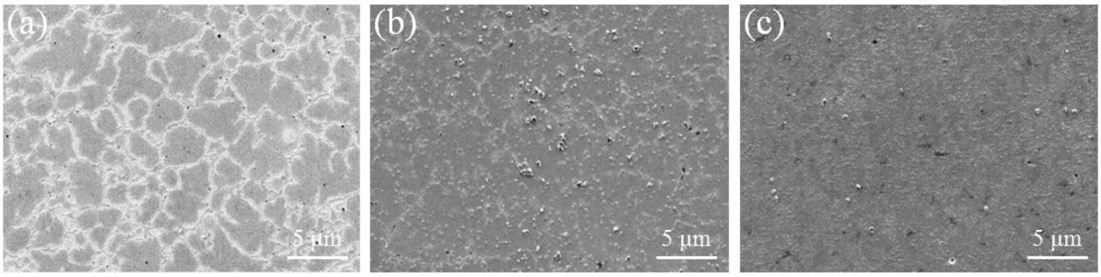

Figure 2. SEM images of surfacing layers with different Nb content (a) 1#; (b) 2#; (c) 3#.

The EDS line scan was used to analyze the composition of the carbide precipitated in the overlay layer. Figure 3 shows the line scan area of the overlay layer and the line scan results. The results show that after the carbide Nb peak, the Ti peak and the C peak line scan intensity increased significantly while the Fe and chromium (Cr) peak weakened, indicating that the carbide mainly contains elemental Nb and Ti.

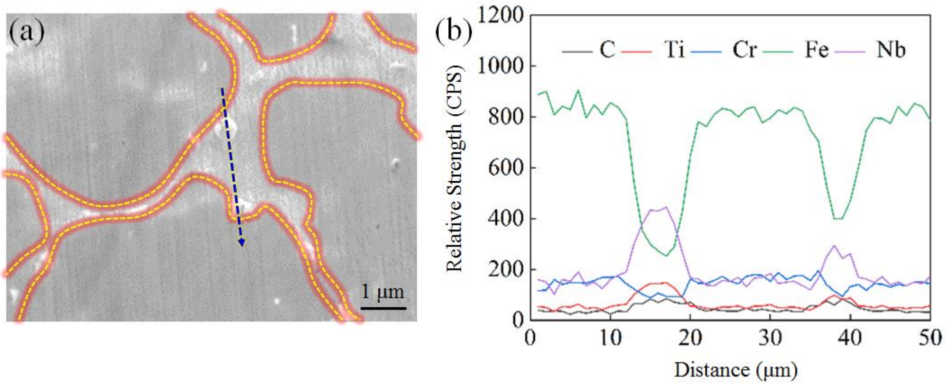

Figure 3. (a) Coating microstructure (the yellow dotted line is the grain boundary interface) and line scanning area (black dotted arrow); (b)EDS line scan pattern of surfacing layers.

3.2 Corrosion resistance

Figure 4 displays the polarization curves for the four samples in the 3.5% NaCl and reveals significant active-passive behavior. Tafel extrapolation was performed from the polarization curves in the first stage of anodic polarization to determine the E_{corr} and I_{corr}, and the results are shown in Table 3. They reveal that the E_{corr} values increase in the order of 1# < 2# < 3#, while the I_{corr} values of the three samples decrease in the order of 1# > 2# > 3#. 3# showing the highest E_{corr} (-0.76 V) and the lowest I_{corr} (3.481 μA·cm^{-2}) than that of the other specimens, indicating that elemental Nb can improve the corrosion resistance of stainless steel coatings.

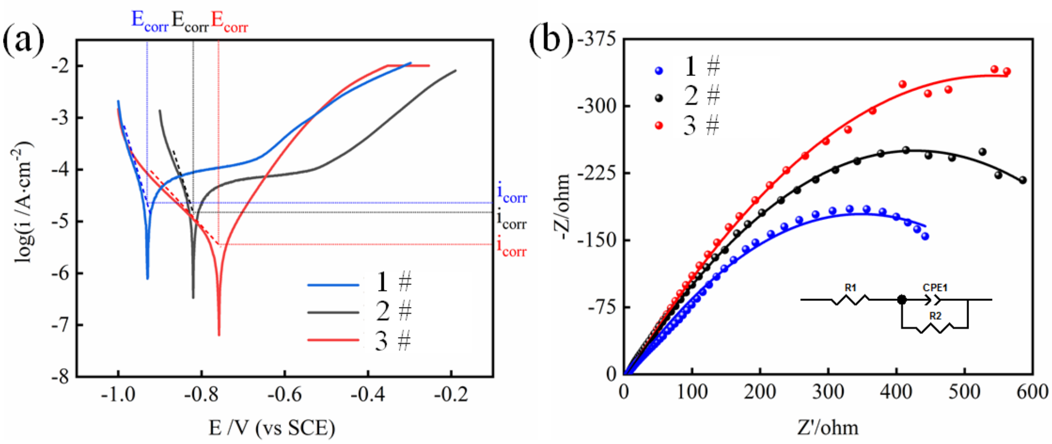

Figure 4. (a) Polarization curves of samples; (b) Nyquist plots of samples (the illustration shows the equivalent circuit, R1 is solution resistance, R2 is coating resistance, CPE1 is Non-ideal capacitance).

Table 3. Corrosion potential E_{corr} and corrosion current density I_{corr} obtained from Tafel extrapolation

Samples	Ecorr /V	Icorr /μA·cm^{-2}
1#	−0.929	22.244
2#	−0.820	14.678
3#	−0.760	3.481

EIS measurements were performed to study the composition of the oxide films in order to investigate the anti-corrosion mechanism of the oxide film on the sample surfaces [22]. As shown in Figure 4b, the impedance spectra are displayed in the form of Nyquist plots. An increase in semicircle diameter indicates an increase in charge transfer resistance or oxide film resistance [23]. To further explore the effect of Nb concentration the corrosion resistance of samples, electrochemical equivalent circuits were suggested in the inset of Figure 4b. In the proposed equivalent circuit, R_1 is the solution resistance, R_2 represent the resistance of oxide layer. The constant phase element (CPE_1) is in place of an ideal capacitance element, and the impedance of the CPE is obtained by equation 2 [24]

$$Z_{CPE} = \frac{1}{Q(j\omega)^n} \tag{2}$$

where, j is the imaginary number and ω is the angular frequency, n is a CPE exponent associated with the roughness and defects on the surface, *CPE* can represent a resistor (n = 0), capacitance (n = 1), Warburg impedance (n = 0.5) or inductance (n = −1) [40]. The values of the equivalent circuit component obtained by fitting the Nyquist curves are shown in Table 4.

It is possible to see that 3# exhibited higher resistance values (183.9 kΩ·cm^2) in comparison to 2# (151.4 kΩ·cm^2) and 1# (127.5 kΩ·cm^2), suggesting that with the increase in Nb content, the corrosion resistance significant increased.

Table 4. Electrical parameters of anodic oxide films by fitting using the equivalent circuit

Samples	R_1 /Ω·cm^2	R_2 /kΩ·cm^2	CPE_1 /μF·cm^{-2}	n_p
1#	6.203	127.5	0.619	0.89
2#	6.199	151.4	0.621	0.91
3#	6.197	183.9	0.618	0.87

Figure 5 is a micrograph of 1 #, 2 #, and 3 # coatings after soaking in 3.5wt% NaCl solution for 30h. Obvious corrosion patterns can be seen on the surface of # 1 # coating under the high magnification effect, accompanied by micron level holes (as shown in Figure 5a). There are no microcracks on the surface of # 2, but under the high magnification effect, the surface still presents obvious corrosion patterns and holes, but the number of holes is less than that of # 1. Observing the 3 # sample (Figure 5c), it could be found that only a small number of micron level holes appear on the coating surface, and there are still no microcracks. Under the high magnification effect, the oxide film surface is very flat, and only a small number of cracks appear.

Calculated from Eq. (1), the corrosion rates of 1#, 2# and 3# coatings were 78.1, 42.8, and 25.2 μm/year, respectively, indicating that the 3 # coating has good corrosion resistance stability.

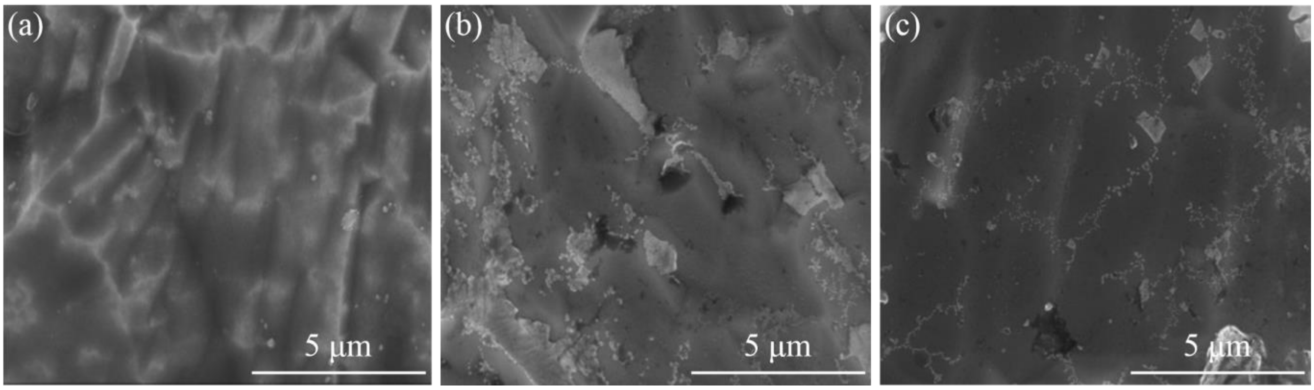

Figure 5. The micrograph of (a) 1 #, (b) 2 #, and (c) 3 # coatings after soaking in 3.5wt% NaCl solution for 30 h

3.3 First-principle calculations

In order to elucidate the mechanism of action of increasing the Nb concentration in enhancing the corrosion resistance of stainless steel, first-principle calculations were performed. To further simplify the model, pure iron was used as the base material. The structure of Fe as shown in Figure 6a, possesses a IM - 3M symmetry (space group OH-9) with an orthogonal lattice, and the optimized lattice parameters for the unit cell of Fe were a = b = c = 2.755 Å, respectively. In general, the stability of low-index crystalline surfaces is stronger than that of higher-index crystalline surfaces. In order to investigate the effect of Nb doping on the stability of different crystalline surfaces of Fe, three low index crystalline surfaces of Fe structure (100), (110) and (111) were selected for this study (Figure 6b).

The surface stability is evaluated by the surface energy, which can be calculated from the chemical potential of Fe atoms according to the thermodynamic relationship for surface energy γ given by Northrup et al. [25]:

$$\gamma = \frac{1}{S_0}\left[E_{slab} - N_{Fe}\mu_{Fe} - PV - TS\right] \tag{3}$$

where S_0 is the surface area (Å^2), E_{slab} is the total energy of the pure surface, N_{Fe} is the number of Fe atoms in the surface system; the chemical potential of Fe is denoted by μ_{Fe}, respectively, and P, V, T, and S denote the pressure, volume, temperature and entropy values of the system, respectively.

At standard atmospheric pressure and absolute zero (T = 0 K), the contribution of and to the Fe surface can be neglected. Therefore, the surface energy can be expressed as:

$$\gamma = \frac{1}{S_0}\left[E_{slab} - N_{Fe}\mu_{Fe}\right] \tag{4}$$

The results of the surface energy calculation are shown in Figure 6c. As an illustration, the Fe(100) plane has the lowest surface energy (-0.029 eV/Å^2) than that of the Fe(110) and Fe(111) plane, the results imply that the Fe(100) plane is the most stable plane.

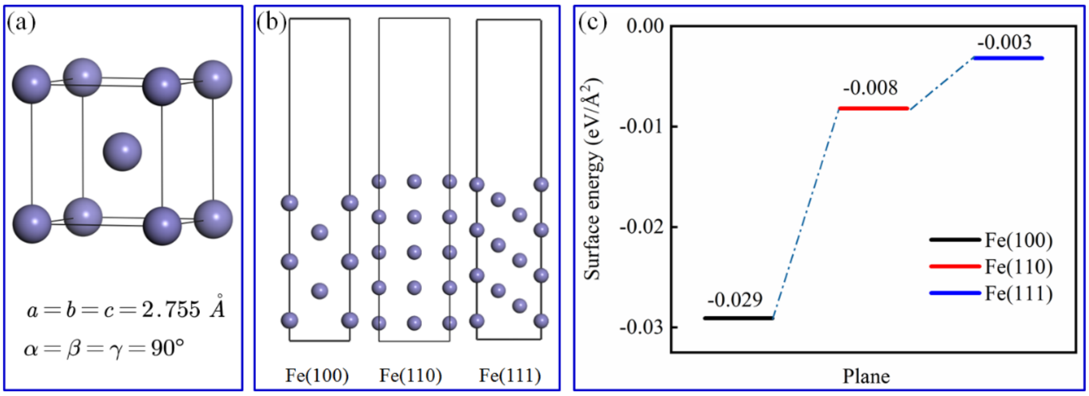

Figure 6. The surface structure and surface energy of Fe: (a) the structure of bulk Fe; (b) the (100), (110) and (111) planes of Fe; (c) the surface energy of Fe surface.

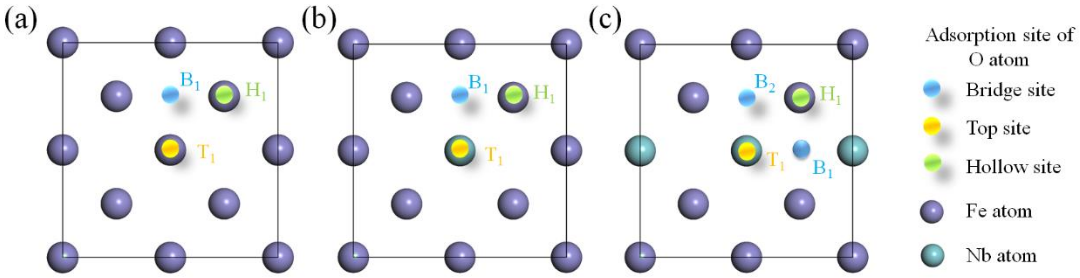

Figure 7. O atoms adsorbed structure on Fe (100) (2 × 2) supercell surface (a) Pure Fe; (b) Fe-1Nb (one Nb atom doped on surface of pure Fe); (c) Fe-2Nb (two Nb atoms doped on surface of pure Fe).

O adsorption at the Fe(100) surface inequivalent sites was used for further studies indicating the corrosion mechanism [6]. According to previous studies, Nb atoms enter the Fe and occupy surface sites, the adsorption structure is shown in Figure 7. Three inequivalent sites exist when the surface coverage of Nb atoms is 0% and 25%, and four inequivalent sites exist when the surface coverage of Nb atoms reaches 50%. In detail, T_1 indicates the top site adsorption at Fe atoms, B_1 - B_2 is the bridge site adsorption, and H_1 is the tetrahedral interstitial site.

The adsorption energy calculation results are shown in Figure 8a. For the pure Fe(100) surface, three stable adsorption sites exist. Among them, the H_1 site has the smallest adsorption energy of -3.945 eV, indicating that the O atom is most easily adsorbed at this site. In contrast, the O atom has the largest adsorption energy (-3.534 eV) when it adsorbs at the top site (T_1) of the Fe atom, indicating that the T_1 site has the lowest adsorption stability. The order of adsorption stability of the three stable O-atom adsorption sites from largest to smallest is: $H_1 > B_1 > T_2$. It is worth noting that the adsorption energy gradually decreases with increasing Nb doping content. When the surface coverage of Nb atoms reaches 50%, the bridge sites have the largest adsorption stability (-2.863 eV). This outcome further illustrates that Nb doping can inhibit formation of dioxides and thus enhance the corrosion resistance of the coatings.

At the same time, the work function of the Nb dope Fe surface needs to be calculated to evaluate the surface electron escape capability [26]. The electrostatic potential of the Nb-doped surface as show in Figure 8b, the red region is negatively charged and is the nucleophilic region. It can be seen that the Nb doping site is in the blue region, indicating that this region is not easily bonded to the O atom. Further comparison of the work functions of the three surfaces shows that the Fe-2Nb surface has the largest work function (4.627 eV). The order of work function of the three surfaces from largest to smallest is: Fe-2Nb > Fe-1Nb > Pure Fe. This result clearly illustrates that Nb doping inhibits the adsorption ability of O atoms on the Fe surface, and the higher its concentration, the greater the enhancement of corrosion resistance on the surface.

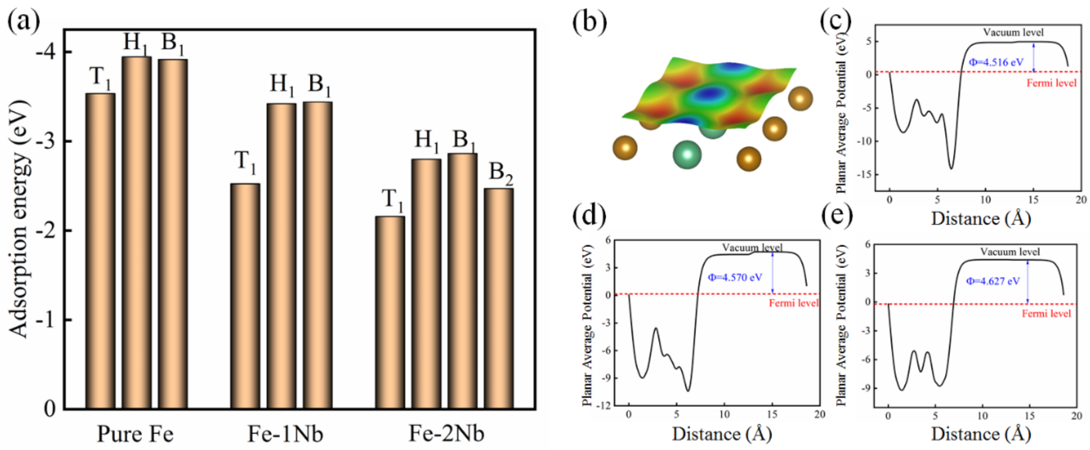

Figure 8. (a) Adsorption energy of O atoms before and after Nb doping; (b) electrostatic potential of Nb-doped surface; (c)-(e) the work function of pure Fe, Fe-1Nb and Fe-2Nb surfaces, respectively.

To further investigate the binding of the Fe surface to O atoms before and after Nb doping, the differential charge density was calculated in this study to characterize the charge distribution of the adsorbed surface and O atoms [27]:

$$\rho(r) = \rho_{O-slab}(r) - \rho_{slab}(r) - \rho_{O}(r) \tag{5}$$

where, $\rho_{O-slab}(r)$ is the charge distribution in the real space of the structure after adsorption, $\rho_{slab}(r)$ is the charge distribution in the real space of the structure before adsorption and $\rho_{O}(r)$ is the charge distribution of the isolated O atoms.

As shown in Figure 9, the cyan area represents a decrease in charge, and the yellow area represents an increase in charge. Comparing the undoped Fe(100) surface and the Nb-doped Fe(100) surface, the real space charge distributions of both have the same trend, and electrons are mainly concentrated around the negatively charged O atoms. However, the yellow area of O atoms on the surface of the Fe(100) surface without Nb doping is larger, indicating that the adsorption capacity of O atoms and the surface decreases after Nb doping. In addition, the Mulliken population analysis [28] was used to analyze the electron transfer between O and the adsorbed surface. The results show that the pure surface has the largest charge transfer (1.028 |e|) than that of Fe-1Nb (0.960 |e|) and Fe-2Nb surface (0.924 |e|). This is consistent with the results for the surface adsorption energy.

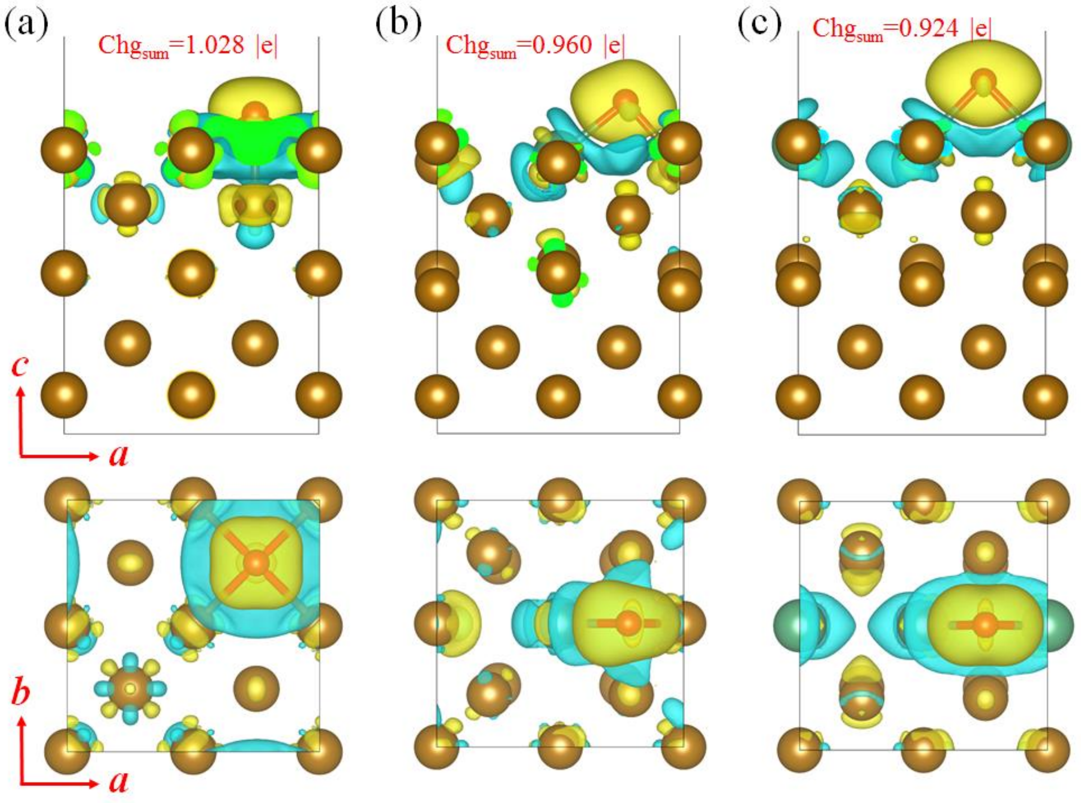

Figure 9. The front and top views of differential charge density of the adsorption surface of (a) pure Fe; (b) Fe-1Nb and (c) Fe-2Nb surface, respectively.

4. CONCLUSIONS

This study has shown that the effect of elemental Nb content on the corrosion resistance of the coating was investigated by generating an iron-based composite overlay layer on Cr5 steel plate using the overlay welding technique. With a further increase in Nb content, the amount of carbide precipitation gradually increases, and the grain boundary of the matrix organization gradually blurs and small grains appear. The number of carbides precipitated in the overlay layer increases gradually with an increase in Nb content. The results of the EDS line scan indicate that the carbide mainly contains elemental Nb and Ti. The electrochemical measurements results showed that 3# showed the highest E_{corr} (-0.76 V) and the lowest I_{corr} (3.481 $\mu A \cdot cm^{-2}$) than that of the other specimens, indicating that elemental Nb can improve the corrosion resistance of stainless steel coatings.

The first-principle calculation results showed that the Fe(100) plane is the most stable plane, and the adsorption energy of the O atom gradually decreases with increasing Nb doping content. When the surface coverage of Nb atoms reaches 50%, the bridge sites have the largest adsorption stability (-2.863 eV). This work function result clearly illustrates that Nb doping inhibits the adsorption ability of the O atoms on the Fe surface, and the higher its concentration, the greater the enhancement of corrosion resistance on the surface.

This work demonstrates that not only evidence of Nb doping can inhibit formation of dioxides of stainless steel and thus enhance the corrosion resistance of the coatings, but also provides a new strategy for improving the corrosion resistance of stainless steel.

ACKNOWLEDGEMENTS
This work was supported by Natural Science Foundation of the Jiangsu Higher Education Institutions of China (21KJB150004), the school-level research projects of Yancheng Institute of Technology (xjr2019028), and Natural Science Foundation of Jiangsu Province (BK20191041).

References

1. E. Sigolo, J. Soyama, G. Zepon, C.S. Kiminami, W.J. Botta and C. Bolfarini, *Surf. Coat. Tech.*, 302 (2016) 255.
2. X.Y. Jin, B. Wang, W.B. Xue, J.C. Du, X.L. Wu and J. Wu, *Surf. Coat. Tech.*, 236 (2013) 22.
3. D. Bowden, Y. Krysiak, L. Palatinus, D. Tsivoulas, S. Plana-Ruiz, E. Sarakinou, U. Kolb, D. Stewart and M. Preuss, *Nat. Commun.*, 9 (2018) 1.
4. H.Q. Xu, J.B. Zang, Y.G. Yuan, P.F. Tian and Y.H. Wang, *Appl. Surf. Sci.*, 492 (2019) 199.
5. E.O. Olakanmi, M. Doyoyo, *J. Therm. Spray Techn.*, 23 (2014) 765.
6. Z. Zhang, T. Yu and R. Kovacevic, *Appl. Surf. Sci.*, 410 (2017) 225.
7. C. Wang, F. Jiang and F. Wang, *Corros. Sci.*, 46 (2004) 75.
8. S.X. Li, Y.N. He, S.R. Yu and P.Y. Zhang, *Corros. Sci.*, 66 (2013) 211.
9. A. Fahim, A.E. Dean, M.D.A Thomas and E.G. Moffatt, *Mater. Corros.*, 70 (2019) 328.
10. V. Firouzdor, K. Sridharan, G. Cao, M. Anderson and T.R. Allen, *Corros. Sci.*, 69 (2013) 281.
11. C. Han, C. Zhang, X. Liu, H. Huang, S.Y. Zhuang, P. Han and X.L. Wu, *J. Mol. Model.*, 21 (2015) 1.
12. B.D.C. Bell, S.T. Murphy, R.W. Grimes and M.R. Wenman, *Acta Mater.*, 132 (2017) 425.
13. X. Yuan, C. Song, X.S. Kong, Y.C. Xu, Q.F. Fang and C.S. Liu, *Physica B*, 425 (2013) 42.
14. D.D. Deshmukh and V.D. Kalyankar, *Int. J. Mater. Prod. Tec.*, 56 (2018) 23.
15. R.W.W. Hsu, C.C. Yang, C.A. Huang and Y.S. Chen, *Mater. Sci. Eng. A*, 380 (2004) 100.
16. M.T. Gorzkowski and A. Lewera, *J. Phys. Chem. C*, 119 (2015) 18389.
17. Y. Wang, C. Li, H. Yang, X. Wang, J.S. Deng and X.H. Yu, *Tribol. Int.*, 154 (2021) 106736.
18. C.H. Zhou, H.T. Ma and L.Wang, *Corros. Sci.*, 52 (2010) 210.
19. L. Wu, T. Guo and T. Li, *J. Mater. Chem. A*, 8 (2020) 19290.
20. L. Chen, T. Yu, P.F. Xu and B. Zhang, *Surf. Coat. Tech.*, 412 (2021) 127027.
21. H.C. Fals, A.S. Roca, J.B. Fogagnolo, L. Fanton, M. J. X. Belém and C. R. C. Lima, *J. Therm. Spray Techn.*, 29 (2020) 319.
22. Y. Chen and W.P. Jepson, *Electrochim. Acta*, 44 (1999) 4453.
23. F. Deflorian, L. Fedrizzi, S. Rossi and P.L. Bonora, *Electrochim. Acta*, 44 (1999) 4243.
24. E.P.M.V. Westing, G.M. Ferrari and J.H.W.D. Wit, *Corros. Sci.*, 34 (1993) 1511.
25. J.E. Northrup, *Phys. Rev. Lett.*, 62 (1989) 2487.
26. J.H. Li, J. Wu, Y.X. Yu, *Appl. Surf. Sci.*, 546 (2021) 149104.
27. A. Sarmah and R.K. Roy. *J. Phys. Chem. C*, 117 (2013) 21539.
28. H.W. Shou, R. Xie, M.J. Peng, Y.H. Duan and Y. *Physica B*, 560 (2019) 41.